



Article

Titanium Nitride Nanodonsuts Synthesized from Natural Ilmenite Ore as a Novel and Efficient Thermoplasmonic Material

Thanh-Lieu Thi Le ¹, Lam Tan Nguyen ¹, Hoai-Hue Nguyen ², Nguyen Van Nghia ¹, Nguyen Minh Vuong ¹, Hoang Nhat Hieu ¹, Nguyen Van Thang ¹, Viet Thong Le ^{2,3}, Viet Huong Nguyen ^{2,3}, Pin-Cheng Lin ⁴, Anupam Yadav ⁴, Ivan Madarevic ⁴, Ewald Janssens ⁴, Hao Van Bui ^{2,3,*} and Loan Le Thi Ngoc ^{1,*}

- ¹ Faculty of Natural Sciences, Quy Nhon University, 170 An Duong Vuong, Quy Nhon City 590000, Vietnam; lethithanhlieu@qnu.edu.vn (T.-L.T.L.); nguyentanlam@qnu.edu.vn (L.T.N.); nguyenvannghia@qnu.edu.vn (N.V.N.); nguyenminhvuong@qnu.edu.vn (N.M.V.); hoangnhathieu@qnu.edu.vn (H.N.H.); nguyenvanthang@qnu.edu.vn (N.V.T.)
- ² Faculty of Electrical and Electronic Engineering, Phenikaa University, Yen Nghia Ward, Ha Dong District, Hanoi 12116, Vietnam; hue.nguyenhoai@phenikaa-uni.edu.vn (H.-H.N.); thong.leviet@phenikaa-uni.edu.vn (V.T.L.); huong.nguyenviet@phenikaa-uni.edu.vn (V.H.N.)
- ³ Faculty of Materials Science and Engineering, Phenikaa University, Yen Nghia Ward, Ha Dong District, Hanoi 12116, Vietnam
- ⁴ Quantum Solid-State Physics, Department of Physics and Astronomy, KU Leuven, 3001 Leuven, Belgium; pincheng.lin@kuleuven.be (P.-C.L.); anupam.yadav@kuleuven.be (A.Y.); ivan.madarevic@kuleuven.be (I.M.); ewald.janssens@kuleuven.be (E.J.)
- * Correspondence: hao.buivan@phenikaa-uni.edu.vn (H.V.B.); lethingocloan@qnu.edu.vn (L.L.T.N.); Tel.: +84-961-960-639 (L.L.T.N.)



Citation: Thi Le, T.-L.; Nguyen, L.T.; Nguyen, H.-H.; Nghia, N.V.; Vuong, N.M.; Hieu, H.N.; Thang, N.V.; Le, V.T.; Nguyen, V.H.; Lin, P.-C.; et al. Titanium Nitride Nanodonsuts Synthesized from Natural Ilmenite Ore as a Novel and Efficient Thermoplasmonic Material. *Nanomaterials* **2021**, *11*, 76. <https://doi.org/10.3390/nano11010076>

Received: 12 December 2020
Accepted: 28 December 2020
Published: 31 December 2020

Publisher's Note: MDPI stays neutral with regard to jurisdictional claims in published maps and institutional affiliations.



Copyright: © 2020 by the authors. Licensee MDPI, Basel, Switzerland. This article is an open access article distributed under the terms and conditions of the Creative Commons Attribution (CC BY) license (<https://creativecommons.org/licenses/by/4.0/>).

Abstract: Nanostructures of titanium nitride (TiN) have recently been considered as a new class of plasmonic materials that have been utilized in many solar energy applications. This work presents the synthesis of a novel nanostructure of TiN that has a nanodonsut shape from natural ilmenite ore using a low-cost and bulk method. The TiN nanodonsuts exhibit strong and spectrally broad localized surface plasmon resonance absorption in the visible region centered at 560 nm, which is well suited for thermoplasmonic applications as a nanoscale heat source. The heat generation is investigated by water evaporation experiments under simulated solar light, demonstrating excellent solar light harvesting performance of the nanodonsut structure.

Keywords: titanium nitride; thermoplasmonic; nanodonsuts; water evaporation

1. Introduction

The emerging field of thermoplasmonics uses metal nanoparticles (NPs) and metal metamaterial structures as nanoscale heat sources when excited at their localized plasmon resonance wavelength through incident light absorption [1,2]. This has been employed for various applications, such as cancer therapy, photothermal imaging, photothermal and hot-electron enhanced chemistry, and applications based on solar light harvesting [3].

Solar light is a very important source of environmentally clean and sustainable energy. Thermoplasmonic systems are particularly interesting for solar light harvesting applications, such as thermophotovoltaics and solar water evaporation (SWE). Since ancient times, SWE has been a fundamental technology for potable water production [4,5]. This technology has gained even more attention nowadays due to its great potential for addressing global challenges, such as clean water shortage (e.g., people in remote areas during the flooding season, fisherman on an unexpected long trip on the sea), desalination, and wastewater treatment [6–9]. Generally, in SWE, sunlight is absorbed by a photothermal material (i.e., absorber), which is converted into heat to vaporize water [10]. Due to their broad absorption range, carbon nanomaterials, such as amorphous carbon,

graphene, and carbon nanotubes, are high-efficiency solar light absorbers. Although their low emissivity is a limiting factor for achieving high-efficiency photothermal conversion, various carbon-based materials and structures have demonstrated good SWE performance [9,11–14].

Pioneering research utilizing thermoplasmonics for SWE employed solar harvesting with metal NPs dispersed in a liquid [15–17]. Typically, noble metal NPs, such as Au, Ag, Pt, and Pd, have been employed because of their widespread use in plasmonics and strong light absorption at the localized surface plasmon resonance [10,15,17]. However, their high cost and narrow absorption range are hindrances for practical SWE deployment. Recently, titanium nitride (TiN) has been demonstrated as a highly stable plasmonic material that is much cheaper than noble metals [18–25]. TiN NPs have been reported to be promising for solar harvesting applications, in which efficient nanoscale heat generators with a wide spectral absorption range are highly desirable [21,26,27]. Employing these advantages, TiN has been demonstrated as an excellent photothermal material for SWE [21–23,28–30]. Furthermore, since evaporation occurs at the liquid–air interface, and heat is generated in the bulk liquid, the volumetric heating method usually achieves low energy conversion efficiency due to the heat loss [5,28]. Therefore, recent SWE studies have employed floating structures, in which the photothermal material is immobilized on a substrate that floats in water. Using this approach, significant improvements of the SWE efficiency have been achieved [9,11,14,30–32].

In this work, we present a low-cost method for fabricating a novel nanostructure of TiN, i.e., nanodonut. The TiN nanodonuts exhibit strong and spectrally broad localized surface plasmon resonance absorption in the visible region that provides excellent photothermal conversion performance. We demonstrate the effectiveness of the TiN nanodonuts as broad-band thermoplasmonic heat generators for SWE under simulated solar light using the floating substrate approach by depositing the TiN nanodonuts on a polymer membrane.

2. Experimental Section

2.1. Materials and Chemicals

Ammonium hydroxide (NH₄OH, 25%), hydrofluoric acid (HF, 48%), potassium chloride (KCl, 99%), and carbon nanopowders (average diameter of 100 nm) were purchased from Sigma-Aldrich Co., Ltd. (St. Louis, MO, USA). Ilmenite ore with the chemical composition 49.5% TiO₂, 32.7% Fe₂O₃, 11.2% FeO, 0.2% SiO₂ and 6.4% other impurities was provided by Binh Dinh Minerals Joint Stock Co., Vietnam.

2.2. Synthesis of TiO₂ Nanoparticles from Ilmenite Ore

TiO₂ NPs were synthesized by a three-step process described as follows:

Step 1: Ilmenite ore was firstly crushed and ground into fine powder with particle sizes in the range of 50–75 μm. Then, 10 g of the powder was transferred into a 250 mL plastic beaker containing 70 mL of HF 20% solution. The suspension was continuously stirred for 5 h at room temperature. The obtained slurry suspension (i.e., filtrate) was separated from the deposited solid residual.

Step 2: 30 mL KCl 4 M solution was slowly added to the filtrate, resulting in a white K₂TiF₆ precipitate. In the next step, the precipitate was separated and dissolved in water by heating up the suspension to 80 °C until a saturated solution was achieved, which was then filtered and rapidly cooled down to room temperature to form again K₂TiF₆ precipitate. This step was used to eliminate the impurities and purify the K₂TiF₆ precipitate. The precipitate was dried in air at 105 °C for 2 h.

Step 3: 5 g of K₂TiF₆ precipitate was dissolved in 500 mL of distilled water by heating up to 80 °C. Then, NH₃ solution (4 M, prepared from ammonium hydroxide 28% solution) was slowly added until pH = 9. This hydrolysis reaction produced Ti(OH)₄, which was then annealed at 550 °C for 3 h to obtain TiO₂.

2.3. Synthesis of TiN by Nitridation of TiO₂ in NH₃

Nitridation of TiO₂ to obtain TiN has been reported by several research groups [33–37]. In our approach, for each experiment, 1 g of TiO₂ NPs was loaded into a ceramic boat and placed at the center of a quartz-tube furnace (PTF 12/50/610, Lenton, UK). One end of the tube was connected to the gas inlet (N₂, NH₃). The other end was connected to a mechanical vacuum pump. Initially, the quartz tube was evacuated to reach a vacuum of 10^{−2} mbar and then pre-heated to 250 °C. The tube was purged several times by N₂ (99.99%) to remove contaminants. Thereafter, the temperature in the furnace was increased to either 700 or 900 °C, both at a ramping rate of 3 °C min^{−1}. After the temperature was stabilized, NH₃ gas was introduced into the furnace at a flow rate of 1000 sccm for 1 h. Finally, the furnace was cooled down to 100 °C in NH₃ ambient, and further to room temperature in N₂ before unloading the sample.

2.4. Material Characterizations

The morphology of the materials was studied by Field-Emission Scanning Electron Microscopy (FE-SEM) and High-Resolution Transmission Electron Microscopy (HR-TEM) using Hitachi S4800 (Ibaraki, Japan) and JEOL ARM-200F (Tokyo, Japan) systems, respectively. The crystalline structure of the materials was investigated by X-Ray Diffraction (XRD) using a Bruker diffractometer (D8 Advance Eco, Bruker, Billerica, MA, USA) equipped with a Cu K α X-ray radiation source. The optical absorption spectra were acquired by using a JASCO V-750 UV-VIS spectrophotometer (Easton, MD, USA). Chemical compositions of the materials and the binding energy of the elements were determined by X-Ray Photoelectron Spectroscopy (XPS) using a XR4 Thermo Scientific Spectrometer (Waltham, MA, USA) equipped with an Mg-K α X-ray radiation source.

2.5. Solar Water Evaporation Experiments

For each experiment, 20 mg of the powder (TiO₂, TiON, TiN or nanocarbon) was dispersed in ethanol and sonicated for 10 min. Using the drop-coating method, the powder was deposited on a polymer membrane (Novatexx 2471, Freudenberg, 5 cm in diameter). The membrane was immersed in water contained in a 100 mL glass beaker and was kept afloat at a distance of ~5 mm below the water surface, which was the equilibrium position of the membrane when it floated. It is worth noting that due to the non-uniform mass distribution, the membrane might be slightly tilted. To address this issue, a thin fabric string was used to keep the entire membrane in the horizontal position. The evaporation was investigated by monitoring the weight change of the system (glass beaker, water and the membrane) under simulated solar light generated by a Xenon arc lamp (60 W, Guangzhou Lightech Auto Lighting Co., Ltd. Guangdong, China) with an illuminance of 550 W m^{−2}, which is equivalent to an illuminance of 0.55 sun of natural solar light. The temperatures of the environment, the surface of the membranes and the liquid were measured using a BETEX 1230 Infrared Thermometer (Bega Special Tools, Vaassen, the Netherlands).

3. Results and Discussion

The hydrofluoric acid leaching of ilmenite ore produces TiO₂ NPs with sizes in the range of 70–160 nm, as shown in the SEM micrograph in Figure 1a. The presence of TiO₂ material is confirmed by XRD and XPS analyses shown in Figures 1d and 1e, respectively. The XRD pattern from the obtained powder (Figure 1d, bottom pattern) is consistent with that of the polycrystalline TiO₂ containing both anatase and rutile phases [38]. The XPS spectrum of the Ti 2p core-level (Figure 1e, bottom spectrum) shows two peaks at binding energies of 464.0 and 458.2 eV. These peaks are the characteristic doublet state of Ti 2p (i.e., Ti 2p_{1/2} and Ti 2p_{3/2}, respectively) in TiO₂ [39]. Following annealing in NH₃ at 700 °C for 1 h, a slight coalescence of the NPs is observed (Figure 1b). The annealing strongly affects the crystalline structure and chemical composition, as shown in the spectra in Figure 1d–f. In the XRD pattern (Figure 1d), the R(110) and A(200) peaks observed for TiO₂ vanish and a new peak at 43.3° appears. This peak represents the (200) plane of TiN cubic structure [40], and is

further confirmed by the HR-TEM image shown in Figure 2a. The co-existence of both TiO_2 and TiN results in the N–Ti–O bonds, causing the broadening of the Ti 2p peaks to the lower binding energy side, as shown in Figure 1e (middle spectrum) [39]. The presence of those bonds is also demonstrated by the broad and asymmetric N 1s peak shown in Figure 1f (middle spectrum) [39]. The XRD and XPS analyses indicate that the nitridation of the TiO_2 at 700 °C was incomplete, resulting in TiO_2 –TiN composite (hereafter denoted as TiON).

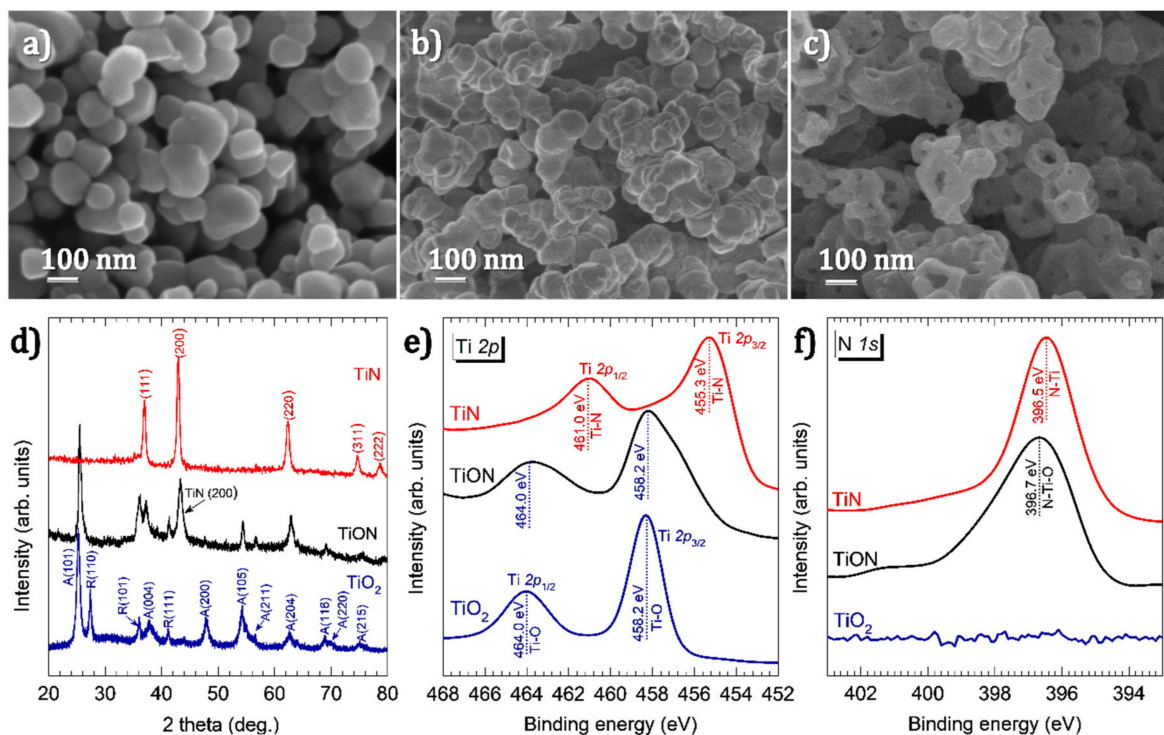


Figure 1. SEM images of (a) the TiO_2 powder obtained directly from the hydrofluoric acid leaching process and (b) after annealing the powder in NH_3 at 700 °C and (c) after annealing at 900 °C; (d) XRD patterns of the powders in images (a–c), labelled as TiO_2 , TiON and TiN, respectively; XPS spectra of TiO_2 , TiON and TiN (e) at the Ti 2p binding energy and (f) at the N 1s binding energy.

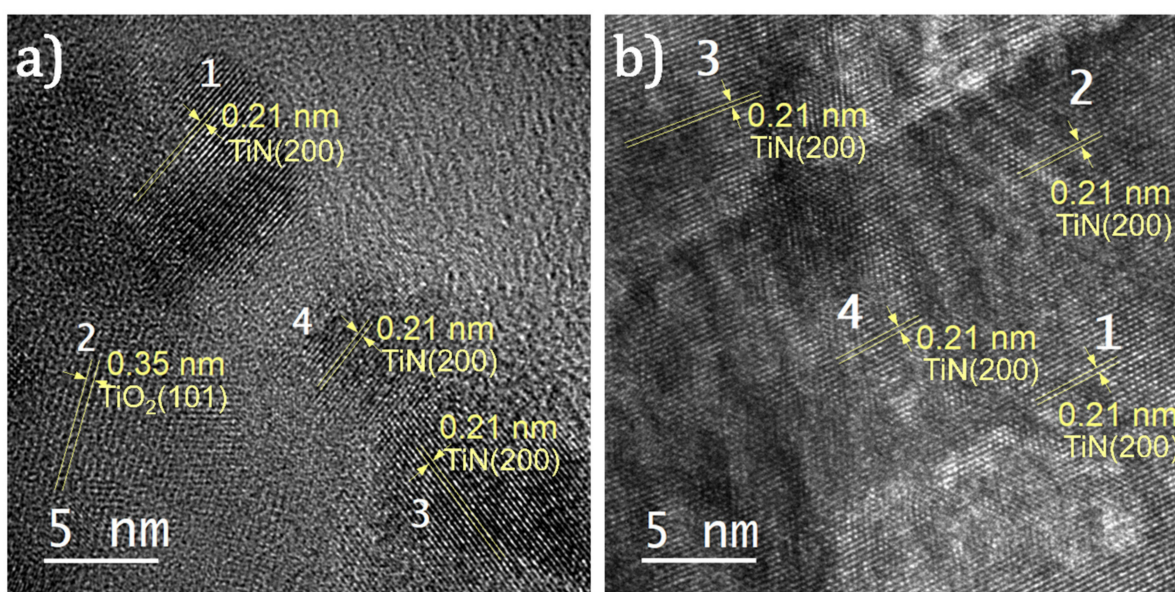


Figure 2. HR-TEM images of (a) TiON and (b) TiN. The lattice spacing was measured using Gatan Micrograph Suite[®] software. The measured lattice spacing of 0.21 nm corresponds to the spacing between (200) planes of TiN, whereas the lattice spacing of 0.35 nm corresponds to the spacing between the (101) planes of anatase TiO_2 [41].

After nitriding at 900 °C in NH₃ for 1 h, the NPs exhibit distinct changes in morphology: the NPs transform into an entirely different structure with the shapes of nanodonuts having outer diameters in the range of 80–120 nm, and inner diameters ranging from 30 to 60 nm (Figure 1c and Figure S1). In the XRD pattern shown in Figure 1d, the diffraction peaks of TiO₂ entirely disappear, and only TiN peaks are observed [27]. This is further supported by the results obtained by HR-TEM shown in Figure 2b. Furthermore, the two peaks at 461.0 and 455.3 eV in the Ti 2p XPS spectrum (Figure 1e) and the peak at 396.5 eV in the N 1s spectrum (Figure 1f) are consistent with the binding energies of Ti–N bonds in stoichiometric TiN [39]. Therefore, we conclude that by annealing in NH₃ at 900 °C, the TiO₂ was completely nitridized and transformed into TiN.

The nitridation of TiO₂ in NH₃ ambient was previously explained by Gou et al. [42]. According to the study, at 900 °C, the nitridation takes place via the formation of TiN_{1-x}O_x and releases H₂O vapor and N₂ gas. With increasing the reaction time, the oxygen atoms of TiN_{1-x}O_x are gradually substituted by the nitrogen atoms. Eventually, TiO₂ is nitridized to TiN [42]. Importantly, the authors observed the formation of mesopores with diameters in the range of 20–40 nm after the nitridation. This is consistent with formation of the cavities, which results in the nanodonuts; this can be attributed to the release of H₂O vapor and N₂ gas. In addition, it has been reported that the incorporation of nitrogen atoms during the nitridation process can cause an expansion and contraction of the particles [43,44], which can be another factor that promotes the formation of the nanodonut structure. Nevertheless, this assumption requires further studies for clarification.

The UV–VIS diffuse reflectance spectra of the materials are shown in Figure 3a. The TiO₂ NPs have an absorption edge at 410 nm, which corresponds to a bandgap of 3.0 eV (using the Tauc method). The absorption of the TiON NPs exhibits a significant red shift that results in a bandgap of 2.1 eV. The TiN nanodonuts manifest a broad plasmon resonance spectrum in the visible region with a peak centered at 560 nm. This is in contrast to resonance peaks commonly observed for TiN, which are in the far-red and near infrared ranges. For instance, Traver et al. reported a peak plasmon resonance at 760 nm for TiN NPs with diameters of 10–20 nm [23]; Ishii et al. reported a peak at 700 nm for TiN NPs with sizes of about 30 nm [27]; whereas Hao et al. reported a peak in the NIR region for the TiN NPs with diameters of 80–90 nm [40]. These examples demonstrate a non-monotonic relationship between the particle size and the plasmon resonance of TiN NPs. We speculate that the peak resonance at 560 nm, in this case, may arise from the structure of the nanodonut NPs, which requires further exploration. Importantly, the broad plasmon resonance spectrum of the TiN nanodonuts corresponds well with the solar spectral range where sunlight provides the highest flux (Figure S2, Supporting Information). This is highly desirable for the solar light harvesting applications.

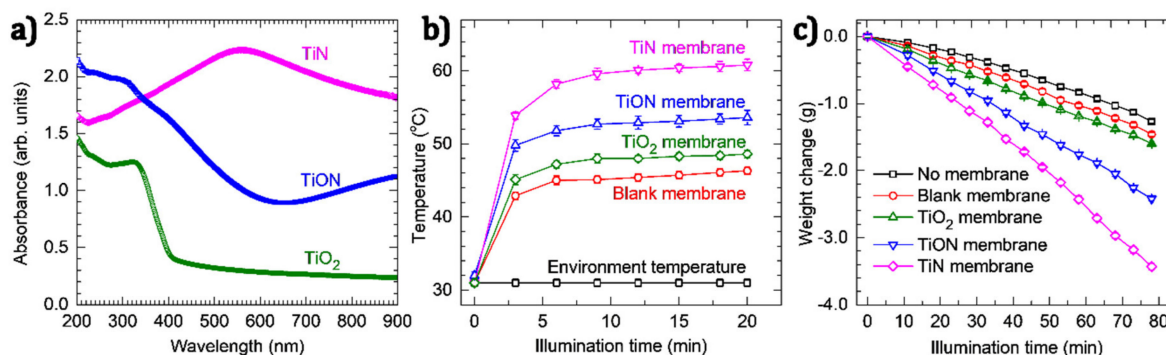


Figure 3. (a) UV–VIS absorption spectra of TiO₂, TiON and TiN nanodonuts, (b) temperature at the surface of membranes under simulated solar light with illuminance of 550 W m⁻², and (c) the weight change due to water evaporation by different photothermal materials.

Figure 3b shows the measured temperatures of the polymer membrane coated with TiO₂, TiON and TiN nanodonuts (hereafter denoted as TiO₂, TiON and TiN membranes,

respectively) under continuous-wave (cw) illumination of simulated solar light generated by a Xenon arc lamp with illuminance of 550 W m^{-2} . The measurements were performed in air at a relative humidity of 72% and an ambient temperature of $31 \text{ }^\circ\text{C}$. The results demonstrate that, after 9 min of cw illumination, the temperature of the blank membrane increases from 31 to $45 \text{ }^\circ\text{C}$ and stabilizes thereafter. Higher temperatures are acquired for the TiO_2 and TiON membranes (i.e., 48 and $53 \text{ }^\circ\text{C}$, respectively), which can be explained by the improved light absorption (Figure 3a). For the TiN membrane, the temperature reaches $60 \text{ }^\circ\text{C}$, indicating its higher photothermal conversion efficiency.

The use of TiN nanodonuts as nanoscale heat generators was tested by studying their SWE performance under cw illumination of simulated solar light with illuminance of 550 W m^{-2} . For this purpose, the membranes were immersed in water and kept at a position of about 5 mm below the water surface. Water evaporation was investigated by monitoring the weight change under continuous cw simulated solar illumination. The results are shown in Figure 3c, demonstrating a linear decrease in weight after 10 min of cw illumination. From these plots, the evaporation rates are calculated, which are presented in Table S1, Supporting Information. For the TiN membrane, an evaporation rate of 0.045 g min^{-1} is achieved. Taking into account the diameter of the glass beaker ($\sim 5 \text{ cm}$) gives an evaporation rate of $1.38 \text{ kg h}^{-1} \text{ m}^{-2}$. This rate is comparable to evaporation rates obtained for various other materials, which are typically in the range of 1.0 – $1.9 \text{ kg h}^{-1} \text{ m}^{-2}$, despite our lower illuminance (Table 1). This suggests the high light harvesting efficiency of the TiN nanodonuts. In addition, the TiN nanodonuts outperform carbon and graphene NPs under similar experimental conditions (Table S1 and Figure S3, Supporting Information). Furthermore, it is worth mentioning that the TiN membrane was used for a considerable number of experiments (i.e., above 30) in various experimental conditions (e.g., under simulated solar light, under natural solar light, in fresh water and in salt water with a concentration of 35 g L^{-1}) with total illumination time above 30 h. The data reported in Figure 3c were acquired after the membrane had been used for more than 25 h. No considerable change in the evaporation rate (as well as the formation of air bubbles presented in the next part) was observed. This indicates an excellent stability of the TiN nanodonuts.

Table 1. Solar water evaporation (SWE) performance of various photothermal materials reported in the literature.

Photothermal Material	Floating Substrate	Light Intensity (kW m^{-2})	Evaporation Rate ($\text{kg h}^{-1} \text{ m}^{-2}$)	Reference
TiN nanodonuts	Polymer membrane	0.55	1.38	This work
TiN NPs	Ceramic fiber wool	1.0	1.847	[21]
TiN NPs	Mesoporous anodized alumina membrane	1.21	1.606	[29]
Ti_2O_3 NPs	Cellulose membrane	1.0	1.32	[45]
RGO-Sodium alginate-CNT aerogel	Self-floating	1.0	1.622	[13]
2D GO film	Cellulose-wrapped Polystyrene foam	1.0	1.45	[46]
Carbon black coated PMMA nanofiber on PAN nanofiber	Self-floating	1.0	1.3	[47]
Bi-layered rGO film	Polystyrene foam	1.0	1.31	[48]
Carbon nanotubes	Porous Silica	1.0	1.32	[49]
Flame-treated wood	Self-floating	1.0	1.05	[50]
Carbonized mushrooms	Polystyrene foam	1.0	1.475	[51]

Importantly, we observed that within 30 s of illumination, bubbles were formed at the TiN membrane surface (Figure 4). Under continuous cw illumination, the bubbles expanded their volume and eventually detached from the membrane surface and moved to the water–air interface, where the air contained in the bubbles was released (Videos S1 and S2, Supporting Information). Only sporadic bubbles were observed for the TiON membrane and no bubble was observed for the blank and the TiO₂ membranes (Figure S4, Supporting Information). This can be explained by the higher temperature of the TiN membrane (i.e., 60 °C), as shown in Figure 3b. The bubble formation due to the thermoplasmonic effect has been described in detail by Baffou et al. [2,52]. Two important conclusions emerge from their analysis: (i) the bubbles contain air, and (ii) the NPs generate a high localized temperature in the range of 200–220 °C, which is required to initiate bubble generation [2,3,52]. From their second conclusion, the bubble formation observed in our work suggests that the local temperature obtained for the TiN nanodonuts under cw illumination could be significantly higher than the measured value at the surface of the TiN membrane (i.e., 60 °C). This seeming discrepancy can be attributed to the fact that the infrared temperature probe has a spot size of about 2 mm and thus provides a spatially averaged value, while the bubble formation occurs locally. We note that bubble formation caused by the thermoplasmonic effect has been observed for Au NPs by many research groups [2,15,17,53]. However, this phenomenon has not been reported for TiN, although high local heat has been suggested for various TiN nanostructures under simulated solar light illumination [19,21,23,27–29].

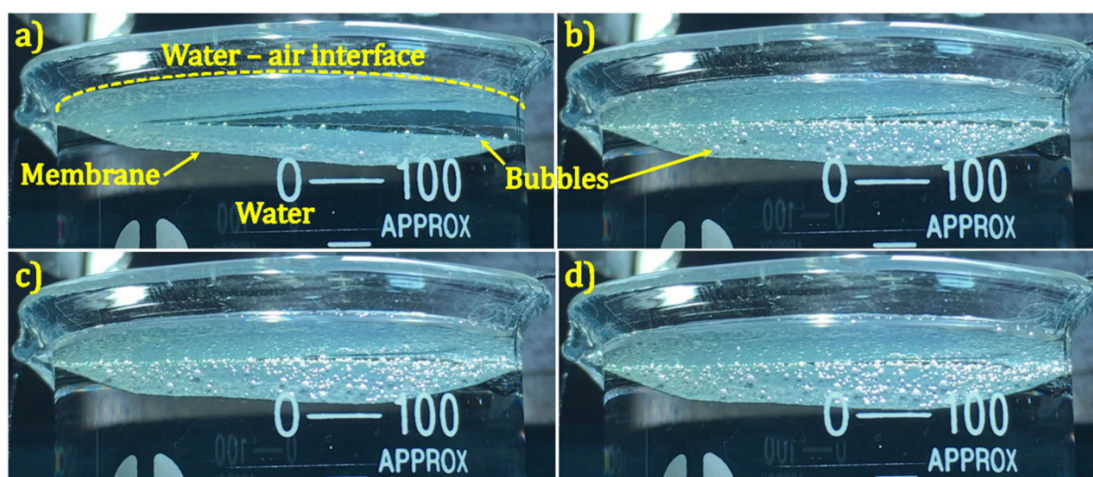


Figure 4. Bubbles generated on TiN membrane surface under continuous illumination for (a) 30 s, (b) 600 s, (c) 1200 s and (d) 1800 s. The membrane is slightly tilted for better observation.

4. Conclusions

In summary, we have demonstrated a low-cost and feasible approach for the fabrication of TiN nanodonuts that exhibit strong and broad plasmon resonance absorption in the visible region centered at 560 nm. The SWE performance was studied using a floating structure prepared by drop-coating the TiN nanodonuts on a polymer membrane. Using simulated solar light with an illuminance of 550 W m⁻², our experiments reveal two important observations. First, the TiN nanodonuts provide an evaporation rate of 1.38 kg h⁻¹ m⁻². This value is comparable to previously reported rates obtained for higher illuminance, proving that the TiN nanodonuts are highly efficient light harvesting materials. Second, the formation of the bubbles at the membrane surface is observed, providing firm evidence of high local heat generated by the TiN nanodonuts, which has not been previously reported.

Supplementary Materials: The following are available online at <https://www.mdpi.com/2079-4991/11/1/76/s1>, Figure S1: Representative TEM images of TiN nanodonuts. The particle and cavity sizes were measured using Gatan Micrograph Suite[®] software, Figure S2: UV-Vis absorption spectrum of TiN nanodonuts and solar emission spectrum, Figure S3: SWE performance of the synthesized photothermal materials (TiO₂, TiON and TiN) in comparison with the graphene nanoplatelets and carbon nanopowders, Figure S4: Photographs of (a) blank polymer membrane, (b) TiO₂ membrane, (c) TiON membrane and (d) TiN membrane taken after 600 s of exposure to simulated solar light generated by the Xenon arc lamp with an illuminance of 550 W m⁻², Table S1: Evaporation rate of water without the membranes, the blank membrane and the membranes deposited with photothermal nanomaterials (TiO₂, TiON, TiN, carbon and graphene NPs) under simulated solar light with an illuminance of 550 W m⁻², Video S1: Formation of bubbles on TiN membrane under continuous illumination of simulated solar light with an illumination of 550 W m⁻², Video S2: Evaporation of water in the presence of the TiN membrane under continuous illumination of simulated solar light with an illumination of 550 W m⁻².

Author Contributions: Conceptualization, L.L.T.N. and H.V.B.; methodology, T.-L.T.L., L.T.N., H.-H.N., N.V.T.; validation, T.-L.T.L., L.T.N., H.-H.N., N.V.T., H.V.B.; formal analysis, H.V.B., L.L.T.N.; investigation, T.-L.T.L., L.T.N., H.-H.N., V.T.L., V.H.N., A.Y., I.M., P.-C.L.; resources, N.V.N., N.M.V., H.N.H., A.Y., I.M., P.-C.L.; data curation, L.L.T.N. and H.V.B.; writing—original draft preparation, L.L.T.N. and H.V.B.; writing—review and editing, L.L.T.N., H.V.B., E.J.; visualization, T.-L.T.L., L.T.N., H.-H.N.; supervision, H.V.B., E.J. and L.L.T.N.; project administration, L.L.T.N.; funding acquisition, L.L.T.N. All authors have read and agreed to the published version of the manuscript.

Funding: This work was financially supported by the Ministry of Education and Training of Vietnam under the grant number B2018-DQN-06.

Acknowledgments: The authors sincerely acknowledge Edwin T. Carlen (Aichmis Technologies, USA) for his valuable comments to the writing of this article. The HR-TEM, XRD and XPS characterizations were supported by the VLIR-UOS South Initiatives Program (Project VN2018SIN239A101).

Institutional Review Board Statement: Not applicable.

Informed Consent Statement: Not applicable.

Data Availability Statement: The data presented in this study are available on request from the corresponding author.

Conflicts of Interest: The authors declare no conflict of interest.

References

1. Baffou, G.; Quidant, R. Thermo-plasmonics: Using metallic nanostructures as nano-sources of heat. *Laser Photonics Rev.* **2013**, *7*, 171–187. [[CrossRef](#)]
2. Baffou, G.; Polleux, J.; Rigneault, H.; Monneret, S. Super-Heating and Micro-Bubble Generation around Plasmonic Nanoparticles under cw Illumination. *J. Phys. Chem. C* **2014**, *118*, 4890–4898. [[CrossRef](#)]
3. Baffou, G.; Cichos, F.; Quidant, R. Applications and challenges of thermoplasmonics. *Nat. Mater.* **2020**, *19*, 946–958. [[CrossRef](#)] [[PubMed](#)]
4. Chen, C.; Kuang, Y.; Hu, L. Challenges and Opportunities for Solar Evaporation. *Joule* **2019**, *3*, 683–718. [[CrossRef](#)]
5. Zhao, F.; Guo, Y.; Zhou, X.; Shi, W.; Yu, G. Materials for solar-powered water evaporation. *Nat. Rev. Mater.* **2020**, *5*, 388–401. [[CrossRef](#)]
6. Tao, P.; Ni, G.; Song, C.; Shang, W.; Wu, J.; Zhu, J.; Chen, G.; Deng, T. Solar-driven interfacial evaporation. *Nat. Energy* **2018**, *3*, 1031–1041. [[CrossRef](#)]
7. Pang, Y.; Zhang, J.; Ma, R.; Qu, Z.; Lee, E.; Luo, T. Solar-Thermal Water Evaporation: A Review. *ACS Energy Lett.* **2020**, *5*, 437–456. [[CrossRef](#)]
8. Yang, P.; Liu, K.; Chen, Q.; Li, J.; Duan, J.; Xue, G.; Xu, Z.; Xie, W.; Zhou, J. Solar-driven simultaneous steam production and electricity generation from salinity. *Energy Environ. Sci.* **2017**, *10*, 1923–1927. [[CrossRef](#)]
9. Ni, G.; Li, G.; Boriskina, S.V.; Li, H.; Yang, W.; Zhang, T.J.; Chen, G. Steam generation under one sun enabled by a floating structure with thermal concentration. *Nat. Energy* **2016**, *1*, 16126. [[CrossRef](#)]
10. Zhu, L.; Gao, M.; Peh, C.K.N.; Ho, G.W. Recent progress in solar-driven interfacial water evaporation: Advanced designs and applications. *Nano Energy* **2019**, *57*, 507–518. [[CrossRef](#)]
11. Ren, H.; Tang, M.; Guan, B.; Wang, K.; Yang, J.; Wang, F.; Wang, M.; Shan, J.; Chen, Z.; Wei, D.; et al. Hierarchical Graphene Foam for Efficient Omnidirectional Solar-Thermal Energy Conversion. *Adv. Mater.* **2017**, *29*, 1702590. [[CrossRef](#)] [[PubMed](#)]

12. Zhang, P.; Liao, Q.; Yao, H.; Cheng, H.; Huang, Y.; Yang, C.; Jiang, L.; Qu, L. Three-dimensional water evaporation on a macroporous vertically aligned graphene pillar array under one sun. *J. Mater. Chem. A* **2018**, *6*, 15303–15309. [[CrossRef](#)]
13. Hu, X.; Xu, W.; Zhou, L.; Tan, Y.; Wang, Y.; Zhu, S.; Zhu, J. Tailoring Graphene Oxide-Based Aerogels for Efficient Solar Steam Generation under One Sun. *Adv. Mater.* **2017**, *29*, 1604031. [[CrossRef](#)] [[PubMed](#)]
14. Ghasemi, H.; Ni, G.; Marconnet, A.M.; Loomis, J.; Yerci, S.; Miljkovic, N.; Chen, G. Solar steam generation by heat localization. *Nat. Commun.* **2014**, *5*, 4449. [[CrossRef](#)] [[PubMed](#)]
15. Fang, Z.; Zhen, Y.R.; Neumann, O.; Polman, A.; De Abajo, F.J.G.; Nordlander, P.; Halas, N.J. Evolution of light-induced vapor generation at a liquid-immersed metallic nanoparticle. *Nano Lett.* **2013**, *13*, 1736–1742. [[CrossRef](#)] [[PubMed](#)]
16. Zeiny, A.; Jin, H.; Lin, G.; Song, P.; Wen, D. Solar evaporation via nanofluids: A comparative study. *Renew Energy* **2018**, *122*, 443–454. [[CrossRef](#)]
17. Neumann, O.; Urban, A.S.; Day, J.; Lal, S.; Nordlander, P.; Halas, N.J. Solar vapor generation enabled by nanoparticles. *ACS Nano* **2013**, *7*, 42–49. [[CrossRef](#)]
18. Li, W.; Guler, U.; Kinsey, N.; Naik, G.V.; Boltasseva, A.; Guan, J.; Shalae, V.M.; Kildishev, A.V. Refractory plasmonics with titanium nitride: Broadband. *Adv. Mater.* **2014**, *26*, 7959–7965. [[CrossRef](#)]
19. Guler, U.; Ndukaife, J.C.; Naik, G.V.; Nnanna, A.G.A.; Kildishev, A.V.; Shalae, V.M.; Boltasseva, A. Local heating with lithographically fabricated plasmonic titanium nitride nanoparticles. *Nano Lett.* **2013**, *13*, 6078–6083. [[CrossRef](#)]
20. Guler, U.; Suslov, S.; Kildishev, A.V.; Boltasseva, A.; Shalae, V.M. Colloidal Plasmonic Titanium Nitride Nanoparticles: Properties and Applications. *Nanophotonics* **2015**, *4*, 269–276. [[CrossRef](#)]
21. Kaur, M.; Ishii, S.; Shinde, S.L.; Nagao, T. All-Ceramic Microfibrous Solar Steam Generator: TiN Plasmonic Nanoparticle-Loaded Transparent Microfibers. *ACS Sustain. Chem. Eng.* **2017**, *5*, 8523–8528. [[CrossRef](#)]
22. Lalis, A.; Tessier, G.; Plain, J.; Baffou, G. Plasmonic efficiencies of nanoparticles made of metal nitrides (TiN, ZrN) compared with gold. *Sci. Rep.* **2016**, *6*, 38647. [[CrossRef](#)] [[PubMed](#)]
23. Traver, E.; Karaballi, R.A.; Monfared, Y.E.; Daurie, H.; Gagnon, G.A.; Dasog, M. TiN, ZrN, and HfN Nanoparticles on Nanoporous Aluminum Oxide Membranes for Solar-Driven Water Evaporation and Desalination. *ACS Appl. Nano Mater.* **2020**, *3*, 2787–2794. [[CrossRef](#)]
24. Guler, U.; Shalae, V.M.; Boltasseva, A. Nanoparticle plasmonics: Going practical with transition metal nitrides. *Mater. Today* **2015**, *18*, 227–237. [[CrossRef](#)]
25. Naik, G.V.; Schroeder, J.L.; Ni, X.; Kildishev, A.V.; Sands, T.D.; Boltasseva, A. Titanium nitride as a plasmonic material for visible and near-infrared wavelengths. *Opt. Mater. Express* **2012**, *2*, 478–489. [[CrossRef](#)]
26. Naldoni, A.; Kudyshev, Z.A.; Mascaretti, L.; Sarmah, S.P.; Rej, S.; Froning, J.P.; Tomanec, O.; Yoo, J.E.; Wang, D.; Kment, Š.; et al. Solar thermoplasmonic nanofurnace for high-temperature heterogeneous catalysis. *Nano Lett.* **2020**, *20*, 3663–3672. [[CrossRef](#)]
27. Ishii, S.; Sugavaneshwar, R.P.; Nagao, T. Titanium Nitride Nanoparticles as Plasmonic Solar Heat Transducers. *J. Phys. Chem. C* **2016**, *120*, 2343–2348. [[CrossRef](#)]
28. Kaur, M.; Ishii, S.; Shinde, S.L.; Nagao, T. All-ceramic solar-driven water purifier based on anodized aluminum oxide and plasmonic titanium nitride. *Adv. Sustain. Syst.* **2019**, *3*, 1800112. [[CrossRef](#)]
29. Bian, Y.; Tang, K.; Xu, Z.; Ma, J.; Shen, Y.; Hao, L.; Chen, X.; Nie, K.; Li, J.; Ma, T.; et al. Highly efficient solar steam generation by hybrid plasmonic structured TiN/mesoporous anodized alumina membrane. *J. Mater. Res.* **2018**, *33*, 3857–3869. [[CrossRef](#)]
30. Zhang, Y.; Li, K.; Liu, L.; Wang, K.; Xiang, J.; Hou, D.; Wang, J. Titanium nitride nanoparticle embedded membrane for photothermal membrane distillation. *Chemosphere* **2020**, *256*, 127053. [[CrossRef](#)]
31. Chen, M.; Wu, Y.; Song, W.; Mo, Y.; Lin, X.; He, Q.; Guo, B. Plasmonic nanoparticle-embedded poly(*p*-phenylene benzobisoxazole) nanofibrous composite films for solar steam generation. *Nanoscale* **2018**, *10*, 6186–6193. [[CrossRef](#)] [[PubMed](#)]
32. Zhu, M.; Li, Y.; Chen, F.; Zhu, X.; Dai, J.; Li, Y.; Yang, Z.; Yan, X.; Song, J.; Wang, Y.; et al. Plasmonic Wood for High-Efficiency Solar Steam Generation. *Adv. Energy Mater.* **2018**, *8*, 1701028. [[CrossRef](#)]
33. Guler, U.; Zemlyanov, D.; Kim, J.; Wang, Z.; Chandrasekar, R.; Meng, X.; Stach, E.; Kildishev, A.V.; Shalae, V.M.; Boltasseva, A. Plasmonic Titanium Nitride Nanostructures via Nitridation of Nanopatterned Titanium Dioxide. *Adv. Opt. Mater.* **2017**, *5*, 1600717. [[CrossRef](#)]
34. Moon, G.D.; Joo, J.B.; Dahl, M.; Jung, H.; Yin, Y. Nitridation and layered assembly of hollow TiO₂ shells for electrochemical energy storage. *Adv. Funct. Mater.* **2014**, *24*, 848–856. [[CrossRef](#)]
35. Samiee, M.; Luo, J. A facile nitridation method to improve the rate capability of TiO₂ for lithium-ion batteries. *J. Power Sources* **2014**, *245*, 594–598. [[CrossRef](#)]
36. Howell, I.R.; Giroire, B.; Garcia, A.; Li, S.; Aymonier, C.; Watkins, J.J. Fabrication of plasmonic TiN nanostructures by nitridation of nanoimprinted TiO₂ nanoparticles. *J. Mater. Chem. C* **2018**, *6*, 1399–1406. [[CrossRef](#)]
37. Romero-Gómez, P.; Rico, V.; Espinós, J.P.; González-Elipé, A.R.; Palgrave, R.G.; Eggedell, R.G. Nitridation of nanocrystalline TiO₂ thin films by treatment with ammonia. *Thin Solid Film.* **2011**, *519*, 3587–3595. [[CrossRef](#)]
38. Duan, Y.; Zhang, M.; Wang, L.; Wang, F.; Yang, L.; Li, X.; Wang, C. Plasmonic Ag-TiO_{2-x} nanocomposites for the photocatalytic removal of NO under visible light with high selectivity: The role of oxygen vacancies. *Appl. Catal. B Environ.* **2017**, *204*, 67–77. [[CrossRef](#)]
39. Oktay, S.; Kahraman, Z.; Urgan, M.; Kazmanli, K. XPS investigations of tribolayers formed on TiN and (Ti, Re)N coatings. *Appl. Surf. Sci.* **2015**, *328*, 255–261. [[CrossRef](#)]

40. Hao, Q.; Li, W.; Xu, H.; Wang, J.; Yin, Y.; Wang, H.; Ma, L.; Ma, F.; Jiang, X.; Schmidt, O.G.; et al. VO₂/TiN Plasmonic Thermo-chromic Smart Coatings for Room-Temperature Applications. *Adv. Mater.* **2018**, *30*, 1705421. [[CrossRef](#)]
41. Xie, Z.; Liu, X.; Zhan, P.; Wang, W.; Zhang, Z. Tuning the optical bandgap of TiO₂-TiN composite films as photocatalyst in the visible light. *AIP Adv.* **2013**, *3*, 062129. [[CrossRef](#)]
42. Gou, H.P.; Zhang, G.H.; Chou, K.C. Phase evolution and reaction mechanism during reduction–nitridation process of titanium dioxide with ammonia. *J. Mater. Sci.* **2017**, *52*, 1255–1264. [[CrossRef](#)]
43. Al-Thabaiti, S.A.; Hahn, R.; Liu, N.; Kirchgeorg, R.; So, S.; Schmuki, P.; Basahel, S.N.; Bawaked, S.M. NH₃ treatment of TiO₂ nanotubes: From N-doping to semimetallic conductivity. *Chem. Commun.* **2014**, *50*, 7960–7963. [[CrossRef](#)] [[PubMed](#)]
44. Shin, H.; Kim, H., II; Chung, D.Y.; Yoo, J.M.; Weon, S.; Choi, W.; Sung, Y.E. Scaffold-like titanium nitride nanotubes with a highly conductive porous architecture as a nanoparticle catalyst support for oxygen reduction. *ACS Catal.* **2016**, *6*, 3914–3920. [[CrossRef](#)]
45. Wang, J.; Li, Y.; Deng, L.; Wei, N.; Weng, Y.; Dong, S.; Qi, D.; Qiu, J.; Chen, X.; Wu, T. High-Performance Photothermal Conversion of Narrow-Bandgap Ti₂O₃ Nanoparticles. *Adv. Mater.* **2017**, *29*, 1603730. [[CrossRef](#)]
46. Li, X.; Xu, W.; Tang, M.; Zhou, L.; Zhu, B.; Zhu, S.; Zhu, J. Graphene oxide-based efficient and scalable solar desalination under one sun with a confined 2D water path. *Proc. Natl. Acad. Sci. USA* **2016**, *113*, 13953–13958. [[CrossRef](#)]
47. Xu, W.; Hu, X.; Zhuang, S.; Wang, Y.; Li, X.; Zhou, L.; Zhu, S.; Zhu, J. Flexible and Salt Resistant Janus Absorbers by Electrospinning for Stable and Efficient Solar Desalination. *Adv. Energy Mater.* **2018**, *8*, 1702884. [[CrossRef](#)]
48. Shi, L.; Wang, Y.; Zhang, L.; Wang, P. Rational design of a bi-layered reduced graphene oxide film on polystyrene foam for solar-driven interfacial water evaporation. *J. Mater. Chem. A* **2017**, *5*, 16212–16219. [[CrossRef](#)]
49. Wang, Y.; Zhang, L.; Wang, P. Self-Floating Carbon Nanotube Membrane on Macroporous Silica Substrate for Highly Efficient Solar-Driven Interfacial Water Evaporation. *ACS Sustain. Chem. Eng.* **2016**, *4*, 1223–1230. [[CrossRef](#)]
50. Xue, G.; Liu, K.; Chen, Q.; Yang, P.; Li, J.; Ding, T.; Duan, J.; Qi, B.; Zhou, J. Robust and Low-Cost Flame-Treated Wood for High-Performance Solar Steam Generation. *ACS Appl. Mater. Interfaces* **2017**, *9*, 15052–15057. [[CrossRef](#)]
51. Xu, N.; Hu, X.; Xu, W.; Li, X.; Zhou, L.; Zhu, S.; Zhu, J. Mushrooms as Efficient Solar Steam-Generation Devices. *Adv. Mater.* **2017**, *29*, 1606762. [[CrossRef](#)] [[PubMed](#)]
52. Baffou, G. *Thermoplasmonics: Heating Metal Nanoparticles Using Light*; Cambridge University Press: Cambridge, UK, 2018; ISBN 978-1-108-41832-4.
53. Carlson, M.T.; Green, A.J.; Richardson, H.H. Superheating water by CW excitation of gold nanodots. *Nano Lett.* **2012**, *12*, 1534–1537. [[CrossRef](#)] [[PubMed](#)]